

Elasticity of quasi-bcc ammonia hemihydrate at high pressures

Mengqiong Pu(蒲梦琼), Jiacheng Zhang(张家诚), Xinyang Li(李新阳), Xiaomei Yuan(苑晓美), Xue Zhang(张雪), Shuo Gao(高硕), Chenlu Wang(王晨璐), Liang Li(李亮), Fangfei Li(李芳菲), and Qiang Zhou(周强)

Citation: Chin. Phys. B, 2026, 35 (**3**): 036101. DOI: 10.1088/1674-1056/ae330a
http://cpb.iphy.ac.cn; http://iopscience.iop.org/cpb

What follows is a list of articles you may be interested in

Pressure-induced amorphization and metallization in orthorhombic SiP

Qiru Zeng(曾琪茹), Youjun Zhang(张友君), Yukai Zhuang(庄毓凯), Linfei Yang(杨林飞), Qiming Wang(王齐明), and Yi Sun(孙熠)

Chin. Phys. B, 2025, 34 (**9**): 096102. DOI: 10.1088/1674-1056/add4f6

First-principles study on structural, electronic, and superconducting properties of Laves-phase alloy $HfZn_2$ under pressure

Xiao Ma(马晓), Tao Wang(王涛), Jianfeng Wen(文剑锋), Zhenwei Zhou(周振玮), and Hongyu Zhu(朱红玉)

Chin. Phys. B, 2025, 34 (**8**): 086108. DOI: 10.1088/1674-1056/ade5a1

Pressure-induced band gap closing of lead-free halide double perovskite $(CH_3NH_3)_2PtI_6$

Siyu Hou(侯思羽), Jiaxiang Wang(王家祥), Yijia Huang(黄乙甲), Ruijing Fu(付瑞净), and Lingrui Wang(王玲瑞)

Chin. Phys. B, 2025, 34 (**8**): 086106. DOI: 10.1088/1674-1056/adce9e

Synergistic improvements in mechanical and thermal performance of TiB_2 solid-solution-based composites

Zhuang Li(李壮), Cun You(由存), Zhihui Li(李志慧), Xuepeng Li(李雪鹏), Guiqian Sun(孙贵乾), Xinglin Wang(王星淋), Qi Jia(贾琪), Qiang Tao(陶强), and Pinwen Zhu(朱品文)

Chin. Phys. B, 2025, 34 (**8**): 086105. DOI: 10.1088/1674-1056/add00c

Morphology-tuned phase transition of MnO_2 nanorods under high pressure

Xue-Ting Zhang(张雪婷), Chen-Yi Li(李晨一), Hui Tian(田辉), Xin-Yue Wang(王心悦), Zong-Lun Li(李宗伦), and Quan-Jun Li(李全军)

Chin. Phys. B, 2025, 34 (**6**): 066105. DOI: 10.1088/1674-1056/adc192

SPECIAL TOPIC — Structures and properties of materials under high pressure

Elasticity of quasi-bcc ammonia hemihydrate at high pressures

Mengqiong Pu(蒲梦琼), Jiacheng Zhang(张家诚), Xinyang Li(李新阳)†, Xiaomei Yuan(苑晓美), Xue Zhang(张雪), Shuo Gao(高硕), Chenlu Wang(王晨璐), Liang Li(李亮), Fangfei Li(李芳菲), and Qiang Zhou(周强)

Synergetic Extreme Condition High-Pressure Science Center, State Key Laboratory of High Pressure and Superhard Materials, College of Physics, Jilin University, Changchun 130012, *China*

(Received 24 November 2025; revised manuscript received 24 December 2025; accepted manuscript online 4 January 2026)

Ammonia hydrates are important components in planetary interiors, among which ammonia hemihydrate (AHH) exhibits remarkable stability under high pressure. In this study, we report for the first time the elastic properties of the recently discovered quasibcc ammonia hemihydrate (AHH-*q*bcc) at high pressures, using externally heated diamond anvil cells combined with Raman spectroscopy and Brillouin scattering. We synthesized single crystals of AHH-*q*bcc in the diamond anvil cell (DAC). Subsequently, we measured its full elastic tensor up to 17.6 GPa at room temperature via Brillouin scattering. The results show that the elastic constants increase linearly with increasing pressure. Based on the obtained elastic constants, we calculated the bulk modulus, shear modulus, Poisson's ratio, and velocity anisotropy. The results reveal significant anisotropy in wave velocities and Poisson's ratio on the (110) crystallographic plane of AHH-*q*bcc. Compared to ice VII, AHH-*q*bcc has a lower bulk modulus and shear modulus, yet exhibits a higher compressional wave velocity and a similar shear wave velocity. Our findings provide important constraints for understanding the internal structure and seismic velocity profiles of icy planets.

Keywords: high pressure, ammonia hemihydrate, Brillouin scattering, Raman spectroscopy

PACS: 61.50.Ks, 07.35.+k, 52.38.Bv, 91.60.Lj

DOI: 10.1088/1674-1056/ae330a **CSTR:** 32038.14.CPB.ae330a

1. Introduction

The outer solar system nebulae, composed of gaseous elements and cosmic dust, contain approximately 15% ammonia and 45% water.[1,2] Ammonia–water mixtures play a prominent role in the interiors of icy planets such as Uranus and Neptune,[3–6] as well as icy moons including Titan, Enceladus, and Ganymede.[7–12] However, ammonia hydrates with lower ammonia concentrations, specifically ammonia trihydrate (ATH), ammonia dihydrate (ADH), and ammonia monohydrate (AMH), fully decompose into ice VII and ammonia hemihydrate-II (AHH-II) at room temperature around 4 GPa.[13–16] Meanwhile, first principles calculations identify AHH as the energetically most stable hydrate under high pressure.[17,18] It is estimated that the mantles of icy giants and planetary nebulae near Saturn consist of about 20% ammonia hemihydrate (AHH) and 80% water ice. Therefore, a comprehensive understanding of AHH phase stability is crucial for determining the internal structure of icy planets and accurately modelling their dynamic behavior.

High-temperature and high-pressure experiments are the primary methods for studying the material composition of Earth's and planetary interiors.[19–21] Studies have revealed that AHH exhibits a complex phase diagram under high pressure and temperature. Below 200 K, the orthorhombic AHH-I phase is stable between 1 bar and 1 GPa.[22] At 300 K, the liquid transforms into monoclinic AHH-II at about 4 GPa.[15,23] Upon further compression to around 26 GPa, a body centered cubic disordered molecular alloy (DMA) phase forms, characterized by random arrangement of ammonia and water molecules on the lattice.[16] Influenced by kinetic barriers, a metastable ordered quasi–bcc phase, denoted as AHH-II*, persists between 26 GPa and 69 GPa. This phase has an ordered structure consisting of two thirds ionic species (NH_4^+, OH^-) and one third molecular NH_3, with space group $P2_1/c$.[24] Andriambariarijaona *et al.* further redefined the DMA phase as AHH-DIMA and confirmed, through x-ray diffraction and Raman spectroscopy combined with visual observation, that AHH-II transforms gradually into the DIMA phase between 25 GPa and 35 GPa.[25] Above 69 GPa, AHH-DIMA transitions into the fully ionic AHH-III phase with space group $P\bar{3}m1$.[24]

Recent studies show that heating AHH-II below 10 GPa and up to 700 K yields a body centered cubic AHH-*p*bcc phase, which represents a plastic form of DIMA exhibiting free molecular rotation.[25] Moreover, in the range of 10 GPa to 19 GPa and 300 K to 450 K, a quasibcc structure denoted as AHH-*q*bcc can be obtained by heating AHH-II above 450 K at about 12 GPa, compressing AHH-*p*bcc above 450 K, or decompressing AHH-DIMA around 19 GPa at 300 K. Once formed at high temperature, AHH-*q*bcc remains stable upon cooling to room temperature and does not revert to AHH-

†Corresponding author. E-mail: lixinyang@jlu.edu.cn

© 2026 Chinese Physical Society and IOP Publishing Ltd. All rights, including for text and data mining, AI training, and similar technologies, are reserved.

II.[25] Although this phase has been identified, its elastic properties under high pressure remain unknown. The combined use of high-pressure techniques and Brillouin spectroscopy represents the most robust approach for determining the elastic properties of materials under extreme compression.[26–35] Therefore, in this study, we employed Brillouin scattering spectroscopy to measure its elastic constants and derived relevant mechanical properties. Our results provide important constraints on the internal structure of icy planets.

2. Methods

2.1. Materials synthesis

We synthesized the sample following the method described in Refs. [23,36]. High-purity ammonia gas (99.99%) was condensed and mixed with distilled water in a molar ratio of 2:1 (NH_3:H_2O) in a hydrothermal autoclave. The mass accuracy of the sample was confirmed to be better than 1% by weighing. The mixture was then loaded into the sample chamber under a liquid nitrogen atmosphere at cryogenic conditions. High-pressure experiments were conducted using a four-pillar diamond anvil cell equipped with diamonds featuring 500 μm culets. A rhenium gasket was used, pre-indented to a thickness of 60 μm, with a 300 μm diameter hole drilled in the center. To prevent reaction between the sample and the gasket material, a gold layer was deposited around the hole as a barrier. Heating was achieved using a Ni–Cr alloy–based ceramic heater, and temperature was monitored with a K-type thermocouple attached approximately 500 μm away from the diamond culet surface. The pressure was determined with the luminescence of ruby spheres using the Ruby2020 calibration.[37] To synthesize AHH-*q*bcc, the sample was first compressed to 3 GPa, then heated to 580 K, followed by further compression to 14 GPa. Formation of AHH-*q*bcc was confirmed in situ using Raman spectroscopy. The resistive heating furnace was then switched off, allowing the sample to cool naturally to room temperature. Single crystals of AHH-*q*bcc were successfully obtained using this procedure. Figure 1 illustrates this synthesis process. We acknowledge that due to weak scattering signals and the unavailability of beamline time at high-energy synchrotron radiation sources (such as at DESY), clear x-ray diffraction data for crystal quality assessment could not be obtained. Therefore, we relied on the clear periodicity in Brillouin scattering as a key indicator of single crystal quality, a method supported by established studies on ice VII.[13,38] Meanwhile, the Brillouin scattering probe area was approximately 50×50 μm^2. Raman spectra collected from the same region confirmed the phase purity within this probed volume.

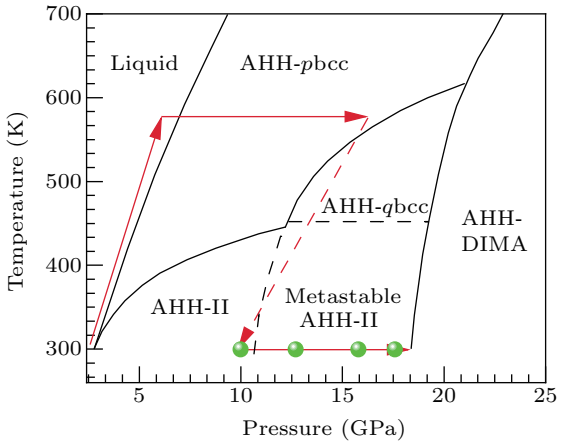


Fig. 1. Synthesis P–T path of AHH-*q*bcc. The phase diagram is adapted from Andriambariarijaona *et al.*[25] Solid red arrows indicate the heating and compression path; dashed arrows represent the cooling path under pressure. Green circles mark the experimental pressure conditions.

2.2. Measurement

High-pressure Raman spectra were collected at room temperature in a backscattering geometry using an Acton SpectraPro 500i spectrometer equipped with a liquid-nitrogen-cooled charge-coupled device (CCD) detector. The 532 nm emission line from a diode-pumped solid-state Nd:Vanadate laser was used as the excitation source. To minimize heating effects, the laser power was maintained at 5 mW at the sample position in the diamond anvil cell.

Brillouin scattering measurements were conducted in symmetric platelet geometry with a scattering angle of 60°. The spectra were recorded using a $3+3$ pass tandem Fabry–Perot interferometer (JRS Scientific Instruments), with excitation provided by a single-longitudinal-mode, frequency-doubled Nd:Vanadate laser operating at 532 nm. Acoustic velocities were determined using the equation

$$v = \frac{\lambda_0 \Delta \upsilon_B}{2\sin(\theta/2)}, \tag{1}$$

where v represents the acoustic velocity, $\Delta\upsilon_B$ denotes the Brillouin frequency shift, λ_0 is the laser wavelength (532 nm), and θ is the external scattering angle (50°). Following the methodology established by Whitfield *et al.*,[39] which demonstrates that acoustic velocities in platelet geometry can be obtained without refractive index correction, we neglected the pressure dependence of the refractive index. Brillouin spectra were acquired at 15° intervals from 0° to 180° at ambient temperature.

3. Results and discussion

The Raman spectrum of synthesized AHH-*q*bcc at 10 GPa is consistent with previously reported results in Fig. 2, confirming that AHH-*q*bcc coexists with AHH–II. This is supported by the persistence of the AHH–II lattice vibration near 260 cm^{-1} and the ν(O–H$\cdots$N) stretching band around 2800–3000 cm^{-1}. Upon compression to 12.7 GPa,

the sample transforms into pure AHH-*q*bcc, as evidenced by the pronounced enhancement of lattice modes at 190 cm^{-1}, 290 cm^{-1}, and 300 cm^{-1}, together with a strong, broadened feature around 3400 cm^{-1}. Further compression to 20 GPa leads to a transition to the AHH–DIMA phase, characterized by a sharp increase in intensity of the N–H stretching modes near 3300 cm^{-1} and the disappearance of the low-frequency peaks at 190 cm^{-1} and 290 cm^{-1}.

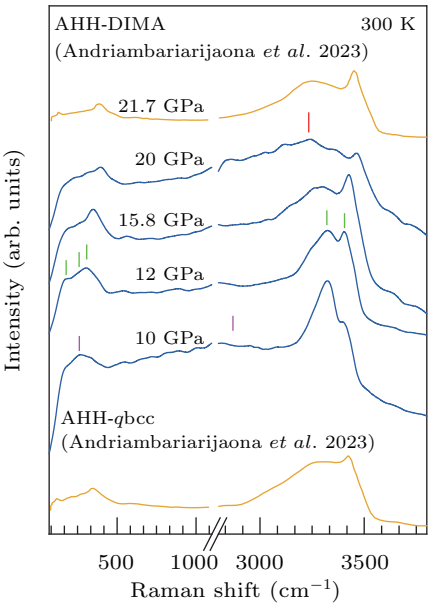


Fig. 2. Representative Raman spectra of AHH. The spectrum shown in orange is reproduced from Ref. [25], while the blue spectrum was obtained in this work. Different phases are labeled accordingly. The purple, green, and red curves are the signatures of AHH–II, AHH-*q*bcc, and DIMA, respectively, emerging during this phase transition.

We measured the elasticity of AHH-*q*bcc under high pressure. Although the crystal structure of AHH-*q*bcc remains under debate, it is considered to adopt a quasi-bcc configuration. Therefore, we described the elastic properties of single-crystal AHH-*q*bcc using a cubic crystal system representation. In the cubic system, there are three independent elastic constants: C_{11}, C_{12}, and C_{44}. These constants were obtained by fitting a set of Christoffel's equations[40] to the measured acoustic velocities

$$|C_{ijkl}n_j n_l - \rho v^2 \delta_{ik}| = 0, \tag{2}$$

where C_{ijkl} is the elastic tensor in full suffix notation (hereafter referred to in the reduced notation C_{ij}), n_j and n_l are direction cosines of the phonon propagation direction, δ_{ik} is the Kronecker delta, ρ is the density, and v is the measured acoustic velocity. Einstein's summation convention is used throughout this article.

Due to the lack of high-pressure density data, we calculated the density information corresponding to the K_S (adiabatic bulk modulus) obtained from Brillouin scattering as follows: First, based on previously reported results, the unit cell volume is 222.21 Å^3,[25] and the volume per formula unit is 18.5175 Å^3. From these values, the density at 12.7 GPa was estimated to be 1.5567 g/cm^3. Using this pressure as a reference point, the density at other pressures was then derived from the equation of state

$$\rho = \rho_0 \exp\left(\int_{P_0}^{P} \frac{1}{K_S} \mathrm{d}P\right), \tag{3}$$

where K_S was calculated using Eq. (4), where ρ_0 is the density at 12.7 GPa and ρ is the density at the respective pressure of interest. It is important to note that Eq. (4), which relates K_S to the elastic constants C_{11} and C_{12}, requires an initial density estimate. Initially, a plausible approximate density was assigned based on the AHH-II equation of state, and the elastic constants were computed using Eq. (2). By comparing the initially assumed density with the resulting calculated values, we iteratively solved Eqs. (2) and (3). The iteration continued until the density converged, at which point the self-consistent density was obtained.

Figure 3 presents representative Brillouin spectra of AHH-*q*bcc measured at 10.0 GPa and 17.6 GPa. At both pressures, distinct peaks corresponding to the longitudinal acoustic mode (V_P) and the two transverse acoustic modes (V_{S1} and V_{S2}) are clearly resolved. With increasing pressure from 10.0 GPa to 17.6 GPa (Fig. 3(a)), all acoustic modes exhibit significant shifts to higher frequencies, indicating a systematic increase in sound velocities. The longitudinal mode V_P shows the most pronounced shift, demonstrating strong stiffening of the crystal under compression. The clear separation between the V_{S1} and V_{S2} modes confirms the elastic anisotropy of the single-crystal AHH-*q*bcc (Fig. 3(b)). The well-resolved peaks and minimal peak broadening at both pressures suggest high sample quality and crystal homogeneity throughout the compression cycle.

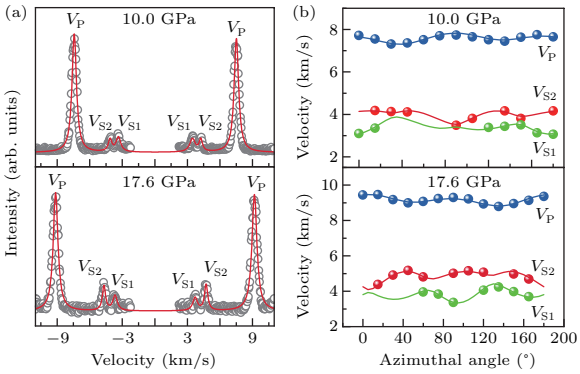


Fig. 3. Representative Brillouin scattering spectra and data fitting results at 10 GPa and 17.6 GPa, measured along the $(-3,1,2)$ and $(-2,1,-1)$ crystal directions, respectively.

Based on the fitting results from Fig. 3(b), we obtained the pressure dependence of the elastic constants C_{11}, C_{12}, and C_{44} for AHH-*q*bcc, which exhibit a nearly linear increase with pressure, as depicted in Fig. 4. Among them, C_{11} exhibits the highest values and the most pronounced pressure dependence, reflecting strong resistance to compression along the principal

axes. The constant C_{12}, associated with lateral stress coupling, also rises steadily, while C_{44}, related to shear rigidity, increases more gradually. The systematic growth of all three elastic constants indicates progressive lattice stiffening under compression and confirms the mechanical stability of the quasi-bcc structure throughout the investigated pressure range.

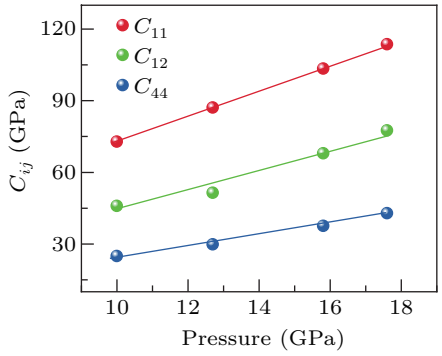


Fig. 4. Pressure dependence of the elastic constants of AHH-*q*bcc.

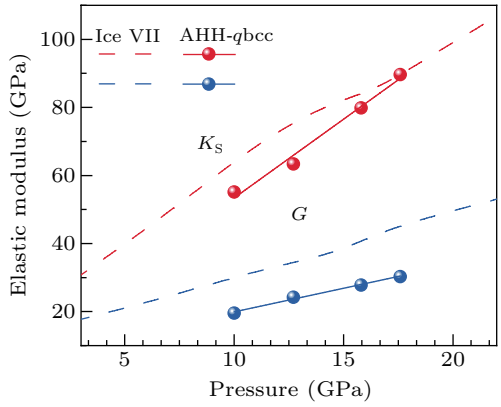


Fig. 5. Pressure dependence of the bulk modulus (K_S) and shear modulus (G) for ice VII and AHH-*q*bcc. Dashed lines represent ice VII from Ref. [13], whereas solid lines correspond to AHH-*q*bcc in this study.

The adiabatic bulk modulus K_S and shear modulus G were also calculated at high pressure (Fig. 5). For a single crystal with cubic symmetry, K_S and G are derived from the obtained elastic constants as follows:

$$K_S = \frac{C_{11}+2C_{12}}{3},\quad G_{Voigt} = \frac{C_{11}-C_{12}+3C_{44}}{5},$$
$$G_{Reuss} = \frac{5(C_{11}-C_{12})C_{44}}{4C_{44}+3(C_{11}-C_{12})}, \tag{4}$$

where G_{Voigt} and G_{Reuss} represent the upper and lower bounds of the shear modulus, respectively.[41] The final shear modulus is taken as the arithmetic mean of the two bounds, known as the Voigt–Reuss–Hill (VRH) average

$$G = \frac{G_{Voigt}+G_{Reuss}}{2}. \tag{5}$$

The calculated bulk modulus (K_S) and shear modulus (G) of AHH-*q*bcc show nearly linear increases within the pressure range of 10–17.6 GPa, reflecting systematic lattice stiffening under high pressure. Compared to ice VII, which also adopts a bcc structure, AHH-*q*bcc exhibits distinct mechanical behavior: its bulk modulus is 0–12.9% lower on average over the studied pressure range, yet converges with that of ice VII at 17.6 GPa. This convergence indicates a stronger pressure dependence of the bulk modulus in AHH-*q*bcc, suggesting that its crystal structure undergoes a different microscopic adjustment mechanism during compression compared to ice VII. More notably, the shear modulus of AHH-*q*bcc is systematically lower than that of ice VII over the entire pressure range, with a significant reduction of 33%–36%. This pronounced difference clearly demonstrates that the incorporation of ammonia molecules fundamentally alters the shear response of the material, markedly weakening the lattice's resistance to shear deformation. This shear softening effect may originate from the specific arrangement of ammonia molecules and their interaction with water molecules in the crystal structure, leading to a substantial weakening of bonding forces along shear directions.

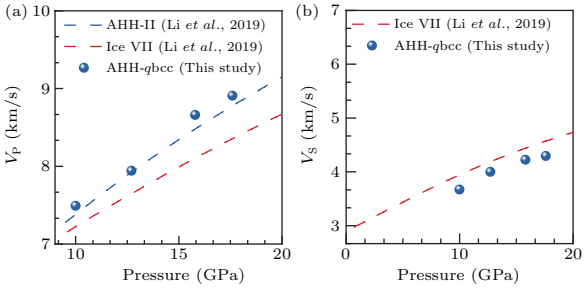


Fig. 6. Isotropic P- and S-wave velocities of AHH-*q*bcc under high pressure. Solid symbols represent sound velocities of AHH-*q*bcc (this study), whereas blue and red dashed lines correspond to AHH-II and ice VII, respectively, from Ref. [13].

Seismic wave velocity measurement is poised to become a primary method for probing the internal structure of icy planets in future deep-space exploration. Using the obtained bulk modulus (K_S) and shear modulus (G), we calculated the acoustic velocities of AHH-*q*bcc based on the following relations:

$$V_P = \sqrt{\frac{K_S+\frac{4}{3}G}{\rho}},\quad V_S = \sqrt{\frac{G}{\rho}}. \tag{6}$$

Both the compressional wave velocity (V_P) and shear wave velocity (V_S) of AHH-*q*bcc increase with pressure, as shown in Fig. 6. Interestingly, although AHH-*q*bcc exhibits lower bulk and shear moduli than ice VII, its compressional wave (V_P) is significantly higher, while shear wave (V_S) remains comparable to that of ice VII (Figs. 6(a) and 6(b)). This apparent contradiction can be explained by the lower density of AHH-*q*bcc, which compensates for its softer elastic moduli and results in higher wave propagation speeds. Furthermore, when compared to another AHH phase, AHH-II (Fig. 6(a)), the compressional wave velocity of AHH-*q*bcc is similar, suggesting that structural differences among AHH polymorphs have a lesser influence on wave speeds than the overall ammonia content.

Consequently, our modeling results indicate that ammonia-rich icy planets may exhibit higher seismic V_P compared to ammonia-poor ones. This insight provides an important indicator for future seismic exploration and interior modeling of icy planetary bodies.

The elastic tensor serves as a fundamental parameter for characterizing the anisotropy of crystalline materials. From the obtained elastic constants and Christoffel's equation, the acoustic wave velocity in any direction of AHH-$q$bcc can be determined. Using the definition $\Gamma_{ik} = C_{ijkl}n_j n_l$ for the 3×3 Christoffel matrix, and defining $\Lambda_{rs} = 3\Gamma_{rs} - \Gamma_{rr}\delta_{rs}$, the homogeneous functions of degree 1, 2, and 3 in the elastic constants C_{ij} are derived as T, G, and H, respectively. Their expressions are[40]

$$\begin{aligned} T &= \Gamma_{rr}, \\ G &= \frac{1}{3}(\Lambda_{12}^2 + \Lambda_{23}^2 + \Lambda_{31}^2 - \Lambda_{22}\Lambda_{33} - \Lambda_{33}\Lambda_{11} - \Lambda_{11}\Lambda_{22}), \\ H &= \frac{1}{2}(\Lambda_{11}\Lambda_{22}\Lambda_{33} + 2\Lambda_{12}\Lambda_{23}\Lambda_{31} - \Lambda_{11}\Lambda_{23}^2 \\ &\quad - \Lambda_{22}\Lambda_{31}^2 - \Lambda_{33}\Lambda_{12}^2), \end{aligned} \tag{7}$$

Thus, the three acoustic velocities corresponding to the modes are derived

$$\begin{aligned} V_P &= \sqrt{\frac{T + 2\sqrt{G}\cos\varphi}{3\rho}}, \\ V_{S1} &= \sqrt{\frac{T + 2\sqrt{G}\cos\left(\varphi + \frac{2}{3}\pi\right)}{3\rho}}, \\ V_{S2} &= \sqrt{\frac{T + 2\sqrt{G}\cos\left(\varphi + \frac{4}{3}\pi\right)}{3\rho}}, \end{aligned} \tag{8}$$

where

$$\varphi = \frac{1}{3}\arccos\left(\frac{H}{G^{3/2}}\right), \tag{9}$$

ρ is the density, V_P is the longitudinal acoustic mode, and V_{S1} and V_{S2} are the two transverse acoustic modes. The results indicate that the compressional wave velocity (V_P) exhibits negligible anisotropy along the [111] direction, while showing mild anisotropy along the [110] and [100] directions (Fig. 7). Notably, this anisotropic behavior remains nearly unchanged with increasing pressure. For shear waves, the fast mode V_{S2} displays strong anisotropy along the [111] and [110] directions, but becomes isotropic in the [100] direction. In contrast, the slow mode V_{S1} shows significant anisotropy in all three crystallographic directions. Similarly, these anisotropic characteristics are largely insensitive to pressure variations.

The observed anisotropy patterns can be attributed to the specific atomic arrangement and bonding environment in the quasi-bcc structure of AHH-$q$bcc. The near-isotropy of V_P along [111] suggests a relatively uniform compressional response in this close-packed direction. The strong shear wave splitting in most directions reflects the structural distortion induced by the incorporation of ammonia molecules, which lowers the symmetry of the ideal bcc lattice and creates distinct shear deformation paths. The pressure-independent nature of the anisotropy indicates that the local bonding topology and molecular orientation remain stable under compression, with the main effect of pressure being a uniform stiffening of all elastic constants without significantly altering the directional dependence of wave propagation.

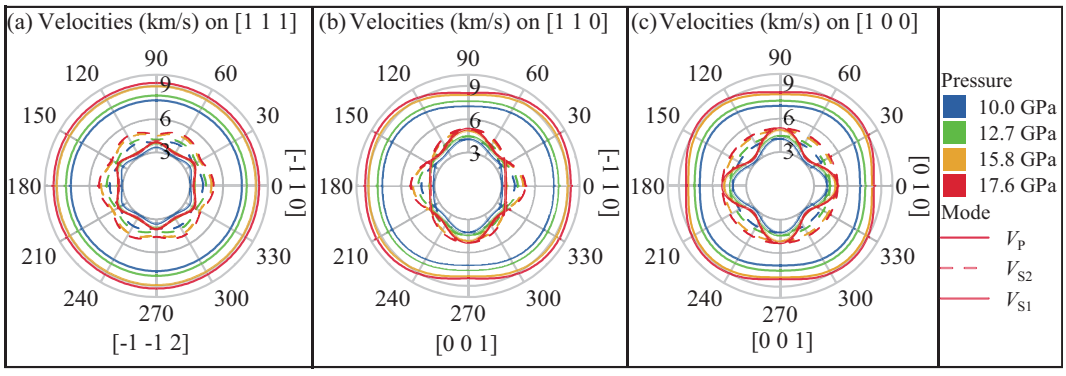


Fig. 7. Velocity anisotropy of AHH-$q$bcc under high pressure along the [111], [110], and [100] crystallographic directions.

The Poisson's ratio serves as a key parameter for characterizing a material's lateral deformation response under axial loading. In planetary science, determining the Poisson's ratio of AHH-$q$bcc provides critical insights into the deformation behavior of icy planetary interiors under gravitational forces, particularly regarding how internal layers may compress or expand differentially under self-gravity or tidal stresses. When calculating the Poisson's ratio along the axial $\vec{n}$ and the transverse $\vec{m}$, it is necessary to convert the stiffness tensor $\boldsymbol{C}$ into the compliance (flexibility) tensor $\boldsymbol{S}$[38,42]

$$\boldsymbol{S} = \boldsymbol{C}^{-1}. \tag{10}$$

The constitutive relationship is

$$\varepsilon_{kl} = S_{klij}\sigma_{ij} = \sigma S_{klij}n_i n_j. \tag{11}$$

Define the strain response matrix A_{kl} resulting from axial stress

$$A_{kl} = S_{klij} n_i n_j, \tag{12}$$

thus, axial strain (ε_{nn})

$$\varepsilon_{nn} = \sigma n_k n_l A_{kl}, \tag{13}$$

the lateral strain (ε_{mm})

$$\varepsilon_{mm} = \sigma m_k m_l A_{kl}, \tag{14}$$

the Poisson's ratio $(\nu_{(n-m)})$

$$\nu_{(n-m)} = -\varepsilon_{mm}/\varepsilon_{nn}, \tag{15}$$

We have calculated the directional dependence of Poisson's ratio for AHH-$q$bcc, as shown in Fig. 8. The results show that along the [111] and [100] crystallographic directions, the Poisson's ratio exhibits negligible anisotropy, with values ranging between 0.25 and 0.31, indicating nearly isotropic lateral deformation in these orientations. In contrast, along the [110] direction, the Poisson's ratio displays strong anisotropy, varying widely from nearly 0 to 0.6 depending on the specific direction within the plane.

This pronounced anisotropy along the [110] direction can be attributed to the layered-like bonding arrangement and anisotropic distribution of intermolecular interactions within the quasi-bcc structure of AHH-$q$bcc. The extremely low Poisson's ratio (near zero) in certain directions suggests that the material exhibits auxetic behavior in these orientations, expanding laterally when stretched, which is likely linked to the hinge-like motion of hydrogen-bonded networks involving ammonia and water molecules. Conversely, the high Poisson's ratio (up to 0.6) in other directions within the same plane indicates exceptionally high compressibility without significant volume change, possibly resulting from sliding of molecular layers or reorientation of molecular dipoles under stress.

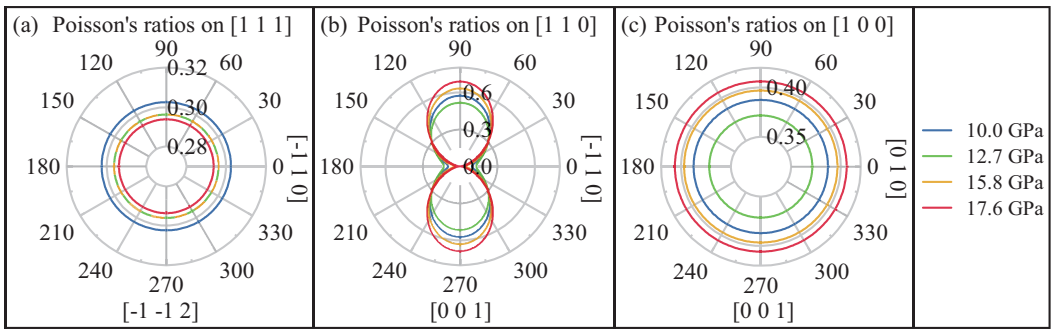


Fig. 8. Anisotropy of Poisson's ratio in AHH-$q$bcc under high pressure along the [111], [110], and [100] crystallographic directions.

If AHH-$q$bcc crystals were preferentially aligned along the [110] direction in planetary interiors, this strong anisotropy in Poisson's ratio could lead to highly heterogeneous deformation patterns under gravitational loading. Such directional deformation behavior might manifest as asymmetric internal structures, anisotropic tidal responses, or influence internal heating through dissipative processes, all of which may have significant implications for the thermal evolution and dynamic behavior of ammonia-rich icy planets and moons. Future work could extend these single-crystal results through texture/polycrystal averaging or deformation experiments to constrain bulk seismic anisotropy in planetary mantles.

4. Conclusion and perspectives

This study presents the first report on the elastic properties of quasi-body-centered cubic ammonia hemihydrate (AHH-$q$bcc) under high pressure, determining its complete elastic tensor up to 17.6 GPa via single-crystal Brillouin scattering measurements. The experimental results demonstrate that all independent elastic constants of AHH-$q$bcc increase linearly with pressure, confirming the mechanical stability of its crystal structure under high-pressure conditions. Compared to ice VII, AHH-$q$bcc exhibits distinctive elastic characteristics: although it possesses lower bulk and shear moduli, it displays higher compressional wave velocity and comparable shear wave velocity due to its significantly lower density. This phase also shows remarkable anisotropy, particularly in shear wave velocities and Poisson's ratio on the (110) plane, revealing strong directional dependence. These findings suggest that if AHH-$q$bcc develops preferred orientation in planetary interiors, it could result in significant seismic anisotropy and heterogeneous deformation patterns. This research provides crucial experimental constraints from mineral physics for understanding the velocity structure and dynamic processes within ammonia-rich icy planets, while its unique elastic characteristics offer important theoretical foundations for future detection of the internal composition and structure of icy planetary bodies.

Acknowledgments

This work was supported by the Synergetic Extreme Condition User Facility (SECUF), the National Natural Science Foundation of China (Grants Nos. 42472065, 12274168, and 42102030), the Jilin Provincial Science and Technology Development Project (Grant No. SKL202502017JC), the Technology Development Plan Project of Changchun, China (Grant No. 2024GZZ06), the Project of "Medical+X" Interdisciplinary Innovation Team of Norman Bethune Health Science Center of Jilin University (Grant No. 2025JBGS03).

References

[1] Lunine J I and Stevenson D J 1987 *Icarus* **70** 61
[2] Guillot T 2005 *Annu. Rev. Earth Planet. Sci.* **33** 493
[3] Ohta K 2023 *Nat. Phys.* **19** 1227
[4] Helled R, Anderson J D, Podolak M and Schubert G 2011 *Astrophys. J.* **726** 15
[5] Teanby N A, Irwin P G J, Moses J I and Helled R 2020 *Phil. Trans. R. Soc. A* **378** 20190489
[6] Helled R, Nettelmann N and Guillot T 2020 *Space Sci. Rev.* **216** 38
[7] Tobie G, Grasset O, Lunine J I, Mocquet A and Sotin C 2005 *Icarus* **175** 496
[8] Waite Jr J H, Lewis W S, Magee B A, Lunine J I, McKinnon W B, Glein C R, Mousis O, Young D T, Brockwell T, Westlake J, Nguyen M J, Teolis B D, Niemann H B, McNutt Jr R L, Perry M and Ip W H 2009 *Nature* **460** 487
[9] Grasset O, Bunce E J, Coustenis A, Dougherty M K, Erd C, Hussmann H, Jaumann R and Prieto-Ballesteros O 2013 *Astrobiology* **13** 991
[10] Sohl F, Solomonidou A, Wagner F W, Coustenis A, Hussmann H and Schulze-Makuch D 2014 *J. Geophys. Res.: Planets* **119** 1013
[11] Fortes A D and Choukroun M 2010 *Space Sci. Rev.* **153** 185
[12] Fagents S A, Lopes R M C, Quick L C and Gregg T K P 2022 *Planetary Volcanism Across the Solar System*, (Amsterdam: Elsevier), pp. 161–234
[13] Li X, Shi W, Liu X and Mao Z 2019 *Am. Mineral.* **104** 1307
[14] Zhang H, Datchi F, Andriambariarijaona L M, Zhang G, Queyroux J A, Beneut K, Mezouar M and Ninet S 2020 *J. Chem. Phys.* **153** 154503
[15] Wilson C W, Bull C L, Stinton G and Loveday J S 2012 *J. Chem. Phys.* **136** 094506
[16] Wilson C W, Bull C L, Stinton G W, Amos D M, Donnelly M E and Loveday J S 2015 *J. Chem. Phys.* **142** 094707
[17] Naden Robinson V, Marques M, Wang Y, Ma Y and Hermann A 2018 *J. Chem. Phys.* **149** 234501
[18] Liu C, Mafety A, Queyroux J A, Wilson C W, Zhang H, Beneut K, Le Marchand G, Baptiste B, Dumas P, Garbarino G, Finocchi F, Loveday J S, Pietrucci F, Saitta A M, Datchi F and Ninet S 2017 *Nat. Commun.* **8** 1065
[19] Zhu J, Feng D, Wang L, Li L, Li F, Zhou Q and Yan Y 2025 *Chin. Phys. B* **34** 066102
[20] Liu Y, Wang Z, Li B, Zhao H, Wang S, Chen L, Ma H and Jia X 2023 *Chin. Phys. B* **32** 128102
[21] Zhao M, Wu B, Liu J and Lei L 2023 *Chin. Phys. B* **32** 090704
[22] Loveday J S and Nelmes R J 2004 *High Pressure Res.* **24** 45
[23] Ma C, Li F, Zhou Q, Huang F, Wang J, Zhang M, Wang Z and Cui Q 2012 *RSC Adv.* **2** 4920
[24] Xu W, Robinson V N, Zhang X, Zhang H C, Donnelly M E, Dalladay-Simpson P, Hermann A, Liu X D and Gregoryanz E 2021 *Phys. Rev. Lett.* **126** 015702
[25] Andriambariarijaona L, Datchi F, Zhang H, Béneut K, Baptiste B, Guignot N and Ninet S 2023 *Phys. Rev. B* **108** 174102
[26] Grimsditch M H and Ramdas A K 1975 *Phys. Rev. B* **11** 3139
[27] Ma C, Wu X, Huang F, Zhou Q, Li F and Cui Q 2012 *J. Chem. Phys.* **137** 104504
[28] Zhang C, Li F, Wei X, Guo M, Wei Y, Li L, Li X and Zhou Q 2022 *Chin. Phys. Lett.* **39** 096201
[29] Ding S, Zhu Y, Liu Y L, Siu G G, Lee C M and Jiang Y J 2005 *Chin. Phys. Lett.* **22** 1790
[30] He X K, Zeng L B, Wu Q S, Zhang L Y, Zhu K and Liu Y L 2012 *Chin. Phys. B* **21** 067801
[31] Xia H, Zhang W, Li Z, Qu X, Chen K and Zhang X 1993 *Chin. Phys. Lett.* **10** 627
[32] Xia H, Peng R, Zhang W, Hu A, Jiang S and Zhang X 1993 *Chin. Phys. Lett.* **10** 569
[33] Shi L W, Duan Y F and Qin L X 2010 *Chin. Phys. Lett.* **27** 080505
[34] Shi X H, Liu B, Yao Z and Liu B B 2020 *Chin. Phys. Lett.* **37** 047101
[35] Wang Z G, Liu Y G, Zhou W G, Song W, Bi Y, Liu L and Xie H S 2013 *Chin. Phys. Lett.* **30** 054302
[36] Pu M, Li X, Yuan X, Geng Y, Ouyang Y, Wang C, Zhang J, Li L, Li F and Zhou Q 2025 *Phys. Rev. B* **111** 174109
[37] Shen G, Wang Y, Dewaele A, Wu C, Fratanduono D E, Eggert J, Klotz S, Dziubek K F, Loubeyre P, Fat'yanov O V, Asimow P D, Mashimo T and Wentzcovitch R M M 2020 *High Pressure Res.* **40** 299
[38] Benedek G B and Fritsch K 1966 *Phy. Rev.* **149** 647
[39] Whitfield C H, Brody E M and Bassett W A 1976 *Rev. Sci. Instrum.* **47** 942
[40] Every A G 1980 *Phys. Rev. B* **22** 1746
[41] Wu Z J, Zhao E J, Xiang H P, Hao X F, Liu X J and Meng J 2007 *Phys. Rev. B* **76** 054115
[42] Marmier A, Lethbridge Z A D, Walton R I, Smith C W, Parker S C and Evans K E 2010 *Comput. Phys. Commun.* **181** 2102